



An Analysis Protocol for Three-Electrode Li-Ion Battery Impedance Spectra: Part I. Analysis of a High-Voltage Positive Electrode

Johannes Landesfeind,^{*,*} Daniel Pritzl,^{*,*,z} and Hubert A. Gasteiger^{**}

Chair of Technical Electrochemistry, Department of Chemistry and Catalysis Research Center, Technical University of Munich, Munich, Germany

A key for the interpretation of porous lithium ion battery electrode impedance spectra is a meaningful and physically motivated equivalent-circuit model. In this work we present a novel approach, utilizing a general transmission line equivalent-circuit model to exemplarily analyze the impedance of a porous high-voltage $\text{LiNi}_{0.5}\text{Mn}_{1.5}\text{O}_4$ (LNMO) cathode. It is based on a LNMO/graphite full-cell setup equipped with a gold wire micro-reference electrode (GWRE) to obtain impedance spectra in both, non-blocking conditions at a potential of 4.4 V cell voltage and in blocking configuration achieved at 4.9 V cell voltage. A simultaneous fitting of both spectra enables the deconvolution of physical effects to quantify over the course of 85 cycles at 40°C: a) the true charge transfer resistance (R_{CT}), b) the pore resistance (R_{pore}), and c) the contact resistance ($R_{cont.}$). We demonstrate that the charge transfer resistance would be overestimated significantly, if the spectra are fitted with a conventionally used simplified R/Q equivalent-circuit compared to our full transmission line analysis.

© The Author(s) 2017. Published by ECS. This is an open access article distributed under the terms of the Creative Commons Attribution Non-Commercial No Derivatives 4.0 License (CC BY-NC-ND, <http://creativecommons.org/licenses/by-nc-nd/4.0/>), which permits non-commercial reuse, distribution, and reproduction in any medium, provided the original work is not changed in any way and is properly cited. For permission for commercial reuse, please email: oa@electrochem.org. [DOI: 10.1149/2.0131709jes] All rights reserved.



Manuscript submitted March 27, 2017; revised manuscript received June 6, 2017. Published June 16, 2017. This was Paper 534 presented at the New Orleans, Louisiana, Meeting of the Society, May 28–June 1, 2017.

Advanced analysis techniques for lithium ion batteries are a key requirement to deconvolute the complex interplay between the aging mechanisms occurring at the anode and the cathode. In principle, this can be accomplished by electrochemical impedance spectroscopy (EIS), if the individual contributions of anode and cathode to the overall cell impedance can be determined, and if this EIS response can be fitted unambiguously to physically motivated equivalent-circuit models. In general, the measured cell and/or electrode impedances are usually fitted with a serial connection of an ohmic resistor (R), with a parallel circuit of a resistor and a capacitor (C), commonly referred to as R/C element and often also modified to an R/Q element (Q representing a constant-phase element), as well as with a Warburg element (W).^{1–5} Recently, more elaborate equivalent-circuits using a transmission line model are getting more and more attention.^{6–8}

In order to independently obtain the impedance of anode and cathode, there are two possible options: i) the assembly of symmetric cells as shown by Chen et al.⁹ or Petibon et al.,¹⁰ where coin cells out of two anodes (impedance of the negative electrode) or two cathodes (impedance of the positive electrode) are assembled in a glove box or dry-room from two (aged) full-cells at a specified state-of-charge (SOC); ii) the use of three-electrode setups consisting of a working electrode (WE), a counter electrode (CE) and a reference electrode (RE), which allows to individually determine the impedance of the anode and the cathode of a lithium ion battery full-cell. The latter is a more convenient approach, as individual impedance spectra can be recorded continuously during battery cycling, so that anode and cathode impedance can be monitored during cycle-life studies on a full-cell instead of obtaining only one set of anode and cathode impedance spectra after disassembly of a full-cell via the symmetric cell approach. A main criterion for a micro-reference electrode suitable for high-quality EIS measurements is a centered position of the reference electrode between working and counter electrode.^{11–13} Several approaches are presented in the literature, as for example, a copper wire, where lithium is in-situ plated from anode or cathode,¹⁴ a reference electrode consisting of a lithium-tin alloy,¹⁵ or consisting of a lithium-bismuth alloy.¹⁶ Our group has recently developed a micro-reference electrode

consisting of a polyimide-shrouded gold wire with a core diameter of 50 μm and an additional 7 μm polyimide insulation layer which enables the deconvolution of full-cell impedances into anode and cathode contributions after lithiation of the gold wire.¹⁷ The latter was used in this study and will be referred to as gold wire reference electrode (GWRE).

Besides the deconvolution of individual electrode impedances, EIS measurements with the GWRE at different states-of-charge of the electrodes allow to get insight into different physical effects. If conducting EIS analysis at a so-called blocking condition for a specific electrode, where no charge transfer reactions (i.e., no faradaic reactions) can take place, the only impedance contribution from the solid-electrolyte interphase is via capacitive coupling. Blocking conditions of electrodes have been used in the literature before to address individual physical processes like the pore resistance and thus the effective ionic conductivity across the thickness of an electrode.^{18,19}

In this work, by using a GWRE and by recording impedance spectra at both blocking and non-blocking conditions, we will demonstrate the ability to deconvolute and quantify the impedance contributions developing during the aging of a high-voltage spinel cathode ($\text{LiNi}_{0.5}\text{Mn}_{1.5}\text{O}_4$ or LNMO) in an LNMO/graphite full-cell cycled at 40°C. For this, we measure half-cell impedance spectra with our GWRE and fit the impedance spectra with a general transmission line model for two distinct points during cycling: i) at 4.4 V cell voltage, corresponding to ~ 7 –12% SOC, where the charge transfer resistance has a typical and reasonably low value; ii) at 4.9 V, where the LNMO is fully delithiated ($\equiv 100\%$ SOC) and where, as we will demonstrate, the LNMO cathode exhibits nearly perfect blocking behavior. The novelty of our approach lies in the fact that by recording both sets of impedance spectra, individual impedance contributions by the LNMO cathode (contact resistance, charge transfer resistance, and pore resistance) can be deconvoluted mathematically and allow for a rather rigorous quantitative analysis during the course of cycle-life experiments. While this is illustrated for the cycling of an LNMO/graphite cell, the general approach shown here is applicable to many other cell chemistries, and the presented analysis of the cathode impedance contributions is also being extended to the anode in our current work. In the following, we will first review the necessary theoretical impedance background, then provide the experimental data, and finally discuss the analysis of the cathode impedance contributions and their variation during cycling.

[†]These authors contributed equally to this work.

^{*}Electrochemical Society Student Member.

^{**}Electrochemical Society Fellow.

^zE-mail: daniel.pritzl@tum.de

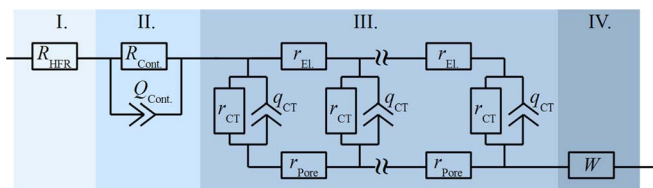


Figure 1. Cathode equivalent circuit model with four parts (from left to right): I. the high frequency resistances from the ionic resistance of the separator and the electronic resistance of the cell setup, II. the contact resistance at the interface between the cathode electrode and its current collector, III. the general transmission line model describing the porous coating, and IV. a Warburg diffusion element.

Theory

The impedance contributions from a porous cathode electrode can be described by a combination of four physical mechanism which are labelled with Roman numerals in the equivalent-circuit depicted in Figure 1 as well as in the simulated Nyquist impedance plot (Figure 2) with parameters given in Table I, using the following assignments: I) the high-frequency resistance (Z_{HFR}), which represents the sum of the ionic resistance of the separator and the electronic resistance of external, electronic cell contacts; II) the contact resistance between the porous electrode and the current collector ($Z_{Cont.}$); III) the impedance contribution from ion and electron conduction across the thickness of the porous cathode electrode (Z_{Pore}), described by the general transmission line model; and, IV) a Warburg diffusion element (Z_W), representing the impedance at very low frequencies. Thus, the overall

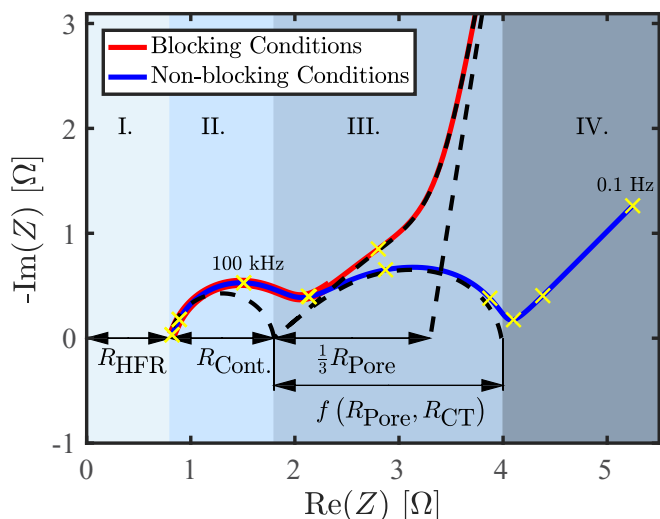


Figure 2. Simulated impedance response of a porous cathode electrode either under blocking conditions (red line) or under non-blocking conditions (blue line), using the parameters listed in Table I for a simulated frequency range from 10 Mhz–0.1 Hz. Each frequency decade is highlighted by a yellow cross. The arrows mark the values of the simulation parameters for the high-frequency resistance (R_{HFR}), the electronic contact resistance ($R_{Cont.}$), and of one third of the pore resistance (R_{Pore}), which are obtained by extrapolating the high- and low-frequency segments of the transmission line response under blocking conditions (dashed black lines). The dashed lines are the modelled impedance responses of only the equivalent-circuit elements in the corresponding region (compare Figure 1), a) the R/Q element due to the contact resistance (region II.), b) the blocking condition transmission line model extending to low frequencies (region III), and, c) the transmission line model in non-blocking condition (region III), and, d) the constant phase behavior of the transmission line model in blocking condition at low frequencies (region III). The frequency range corresponding to the measurement, from 100 kHz to 0.1 Hz is labelled for the reader's convenience.

cathode impedances is:

$$Z_{cathode} = Z_{HFR} + Z_{Cont.} + Z_{Pore} + Z_W \quad [1]$$

In our following measurements with a GWRE (64 μm total diameter) placed in between two glass fiber separators (each with a compressed thickness of $\approx 200 \mu\text{m}$) located between anode and cathode, the impedance at the highest frequencies is composed of the ionic electrolyte resistance in the separator between the cathode/separator interface and the GWRE ($R_{Sep.}$) as well as of the contact resistances from the cell setup (R_{Setup}), adding up to the overall high-frequency resistance, R_{HFR} (compare region I. in Figures 1 and 2):

$$Z_{HFR} = R_{Sep.} + R_{Setup} = R_{HFR} \quad [2]$$

In terms of an equivalent circuit, the overall cathode impedance can thus be described with the equivalent circuit model depicted in Figure 1. The first element starting from the left is R_{HFR} , which is connected in series to the impedance due to contact resistance between the current collector and the positive electrode, described by the $R_{Cont.}/Q_{Cont.}$ element (compare region II. in Figures 1 and 2). The contact resistance circuit element between the cathode current collector and the cathode electrode is a parallel circuit between the interfacial resistance ($R_{Cont.}$) and the generally very small interfacial capacitance (expressed as constant phase element $Q_{Cont.}$), which, based on the definition of the impedance of a constant-phase element ($Z = [Q \cdot (i\omega)^q]^{-1}$), equates to:

$$Z_{Cont.} = \frac{R_{Cont.}}{R_{Cont.} \cdot Q_{Cont.} \cdot (i\omega)^{\alpha_{Cont.}} + 1} \quad [3]$$

with the angular frequency $\omega = 2\pi f$. In this work constant phase elements rather than capacitors are used to account for the non-ideal capacitive behavior commonly observed for the double layer capacitance of porous electrodes.²⁰ The contact resistance is followed by a transmission line equivalent circuit, composed of incremental elements of the charge transfer resistance (r_{CT}), the interfacial double layer capacitance of the cathode (q_{CT}), the purely electronic resistance in the electrode ($r_{El.}$), and the purely ionic resistance in the electrode (r_{ion}) in the mid frequency range (compare region III. in Figures 1 and 2). Thus, the overall charge transfer resistance, the overall electronic and ionic resistances as well as the overall capacitance of the electrode are described by $R_{CT}^{-1} = \Sigma(r_{CT}^{-1})$, $Q_{CT} = \Sigma(q_{CT})$, $R_{El.} = \Sigma(r_{El.})$, and $R_{Pore} = \Sigma(r_{Pore})$. Please note, that the constant phase elements in region II. and region III., namely $Q_{Cont.}$ and q_{CT} , both describe the electrochemical double layer capacitance, $Q_{Cont.}$ at the current collector interface and q_{CT} at the active material and carbon surface respectively.

In this mid-frequency range, the cathode electrode pores dominate the impedance response. In this work, the impedance of the pores is described with a general transmission line model, given by:²¹

$$Z_{Pore} = Z_{||} + Z^* \frac{1 + 2 \cdot p \cdot s \left[\sqrt{1 - \tanh(v)^2} - 1 \right]}{\tanh(v)} \quad [4]$$

with

$$Z_{||} = \frac{Z_P \cdot Z_S}{Z_P + Z_S} \quad [5]$$

$$Z^* = \sqrt{(Z_P + Z_S) \cdot Z_Q} \quad [6]$$

$$p = \frac{Z_P}{Z_P + Z_S} \quad [7]$$

$$s = \frac{Z_S}{Z_P + Z_S} \quad [8]$$

$$v = \sqrt{\frac{Z_P + Z_S}{Z_Q}} \quad [9]$$

Here, Z_S , Z_P , and Z_Q represent the impedances of the electron conducting solid phase of the electrode, of the ionically conducting

pore phase of the electrode, and of the solid/electrolyte interface surfaces within the electrode, respectively. In this work, these elements are described by the electrical resistance throughout the electrode ($Z_S \equiv R_{El}$), by the ionic resistance throughout the electrode ($Z_P \equiv R_{Pore}$), and by an R/Q element describing the coupling for the capacitive elements (Q_{CT}) and of the charge transfer resistance (R_{CT}) at the solid/electrolyte interface surface of the active material in the electrode:

$$Z_Q = \frac{R_{CT}}{R_{CT} \cdot Q_{CT} \cdot (i\omega)^{\alpha_{CT}} + 1} \quad [10]$$

For the commonly considered special case, where the electronic resistance of the electrode is negligible compared to the ionic resistance in the electrode pores (i.e., $R_{El} \ll R_{Pore}$), the transmission line model for the pore impedance (Eqs. 4–9) in blocking conditions ($R_{CT} \rightarrow \infty$) simplifies to Ref. 19:

$$\begin{aligned} Z_{Pore} &= \sqrt{R_{Pore} \cdot Z_Q} \cdot \coth \left(\sqrt{\frac{R_{Pore}}{Z_Q}} \right) \\ &= \sqrt{\frac{R_{Pore}}{Q_{CT} \cdot (i\omega)^{\alpha_{CT}}}} \cdot \coth \left(\sqrt{R_{Pore} \cdot Q_{CT} \cdot (i\omega)^{\alpha_{CT}}} \right) \end{aligned} \quad [11]$$

Finally, the last element represents a Warburg impedance, which generally becomes relevant at very low frequencies (compare region IV. in Figures 1 and 2) and which is connected serially to the transmission line model to account for the salt concentration gradients evolving at low frequencies inside the separator. Please note that this placement of a Warburg diffusion element is not in contradiction with the literature, where a diffusion element is generally connected in series to the charge transfer resistances in order to describe a slow solid-state diffusion process inside the active material particles.^{20,22} In the literature, the solid-state diffusion is generally assumed to be the slowest step (i.e., the one with the longest characteristic time constant), however, as estimated in the Appendix, liquid diffusion through the separator can have a substantially larger impedance, depending on the experimental setup, e.g., the active area or the diffusion coefficient. Thus, with our placement of a Warburg diffusion element in series to the transmission line model we aim at describing the liquid concentration gradients inside the separator.

Only at the very lowest frequencies, a Warburg (W) behavior may be observed, which can be modelled with Ref. 20:

$$Z_W = \frac{W}{\sqrt{\omega}} - i \cdot \frac{W}{\sqrt{\omega}} \quad [12]$$

with the Warburg coefficient W as defined in the Appendix. Generally, the boundary conditions for ionic diffusion in the separator domain will yield a finite, transmissive diffusion behavior for very low frequencies (compare, e.g., Ref. 20, page 102 and following). In this work, no signs of a finite length diffusion were observed in the investigated frequency range (100 kHz to 0.1 Hz), i.e., the decline of the negative imaginary impedance toward the real axis at lowest frequencies in a Nyquist plot, which enables modelling of the separator diffusion with a semi-infinite Warburg diffusion element.

An exemplary evaluation of Equations 1–10 is shown in form of a simulated Nyquist plot in Figure 2 (10 MHz to 0.1 Hz), using the specific parameters for an LNMO cathode listed in Table I, whereby two cases are considered: a) blocking conditions (red line), where R_{CT} becomes very large (ideally going to infinity), here using a value of $R_{CT-blocking}$ of 1 k Ω ; and, b) conditions where a typical value for the charge transfer resistance is observed (blue line), which applies throughout most of the SOC region and which here is given as $R_{CT-non-blocking}$ of 1 Ω . In the first case (red line), the semi-circle for the contact resistance (region II. in Figure 1) can be clearly seen at high frequencies as well as a roughly 45° line produced by the transmission line segment of the circuit shown in Figure 1 (region III.). From this, the value corresponding to one third of the pore resistance (R_{Pore}) can be determined as the difference between the $\text{Re}(Z)$ -axis intercept of the two black dashed lines, which are the extensions of the high- and

Table I. Parameters used in Equations 1–10 for the simulation of the two impedance responses shown in Figure 2, either under blocking conditions where the charge transfer resistance is very large ($R_{CT-blocking}$) or under normal conditions, where a typical value for the charge transfer resistance is used ($R_{CT-non-blocking}$; evaluated at 4.4 V_{FC}). Note that the here chosen values are very similar to the ones which will be found in our later cathode impedance analysis during cycling of an LNMO/graphite cell.

Parameter	Value
R_{HFR}	0.8 Ω
$R_{Cont.}$	1.0 Ω
$Q_{Cont.}$	5 $\mu\text{F} \cdot s^{(\alpha_{Cont.}-1)}$
$a_{Cont.}$	0.9
R_{Pore}	4.5 Ω
R_{El}	1 m Ω
$R_{CT-non-blocking}$	1.0 Ω
$R_{CT-blocking}$	1 k Ω
Q_{CT}	1 mF $\cdot s^{(\alpha_{CT}-1)}$
a_{CT}	0.9
W	1 Ω/\sqrt{s}

low-frequency segments of the transmission line part (region III.) of the equivalent circuit shown in Figure 1. This is derived from the low-frequency limit of Eq. 4, assuming a negligible electronic resistance ($R_{El} \sim 0$), as explained, e.g., in Ref. 20 (p. 207, Eq. 9.11). The difference between the left dashed line intersecting with the $\text{Re}(Z)$ -axis and the high-frequency resistance intersect is the value of the contact resistance ($R_{Cont.}$).

Under non-blocking conditions (blue lines), two semi-circles appear across regions II and III in Figure 2 (plus the onset of the Warburg diffusion branch at low frequencies in region IV), and the low-frequency semi-circle now corresponds to a complex convolution (not simply additive) of the pore ionic conduction and the charge transfer resistance (marked by the arrow labelled $f(R_{Pore}, R_{CT})$). In the most general case, also the magnitude of the electronic resistance influences the shape of the transmission line part (region III. in Figures 1 and 2) but can be neglected when it is much smaller than the ionic resistance inside the pore. The simulated transmission line segment under non-blocking conditions (see region III in Figure 1 with finite R_{CT}) is shown as the dashed semi-circle at low frequencies in Figure 2. Quite clearly, if one were to fit two semi-circles and a Warburg element to the blue EIS response under non-blocking conditions, the diameter of the semi-circle at low-frequencies, which is commonly ascribed to the charge transfer resistance,^{23,24} would indeed be much larger than the actual charge transfer resistance (ca. 2.5 Ω as can be seen from Figure 2 in contrast to the 1 Ω (see Table I) which was used in the model). Therefore, as we will illustrate in the Results and discussion section, a quantification of the charge transfer resistance requires impedance spectra at both blocking and non-blocking conditions for an unambiguous assignment. For a better comparison with our experimental data, which were limited to an upper frequency of 100 kHz due to experimental reasons (see Experimental section), each frequency decade of the blocking and the non-blocking equivalent-circuit simulations (from 10 MHz to 0.1 Hz) in the simulations shown in Figure 2 is marked by a yellow cross (the maximum experimental frequency of 100 kHz is labeled in the figure).

Experimental

Electrode preparation.—Cathodes were prepared from $\text{LiNi}_{0.5}\text{Mn}_{1.5}\text{O}_4$ powder (LNMO, BASF SE, Germany), polyvinylene difluoride (PVdF HSV 900, Kynar), and carbon black (SuperC65, Timcal). The powders were mixed in a mass ratio of 92:3:5 (LNMO:PVdF:carbon black) and dissolved in NMP (N-methyl pyrrolidone, anhydrous, Sigma Aldrich, Germany), followed by three sequential mixing steps with a planetary mixer (Thinky Corp.) for a total of 15 minutes. The final ink, which had a solid content

of 60%, was coated on the rough side of an aluminum foil (MTI, thickness $\sim 18 \mu\text{m}$) at a wet film thickness of $\sim 200 \mu\text{m}$ with a doctor blade coating device (RK PrintCoat Instruments, UK). The resulting loading of the electrodes was $\sim 13 \text{ mg}_{\text{LNMO}}/\text{cm}^2_{\text{Electrode}}$ corresponding to $\sim 1.9 \text{ mAh}/\text{cm}^2_{\text{Electrode}}$ based on a theoretical capacity of $140 \text{ mAh}/\text{g}_{\text{LNMO}}$. The electrodes were punched out with a diameter of 11 mm and afterwards compressed to a porosity of $\sim 32\%$ using a KBr press (Mauthe, PE-011).

Anodes were prepared from Graphite powder (commercial, SGL Carbon GmbH) and PVdF with a mass ratio of 95:5. The mixing procedure was identical to the cathodes. The ink (60% solid content) was coated on the rough side of a copper foil (MTI, thickness $\sim 12 \mu\text{m}$). The electrodes were punched out with a diameter of 11 mm and compressed to a porosity of $\sim 32\%$. The final loading was $6.6 \text{ mg}_{\text{Graphite}}/\text{cm}^2_{\text{Electrode}}$, corresponding to $\sim 2.3 \text{ mAh}/\text{cm}^2_{\text{Electrode}}$ based on a theoretical capacity of $\sim 340 \text{ mAh}/\text{g}_{\text{Graphite}}$.

Anode and cathode coatings were dried in a convection oven at 50°C for at least 3 h. The as-prepared electrodes (graphite anodes and LNMO cathodes) were vacuum dried for at least 12 h at 120°C in a vacuum oven (Büchi, Switzerland) and transferred into an Argon-filled glove box without exposure to air.

Cell assembly and testing.—Spring-compressed (at ~ 1 bar) T-cells (Swageklok, U.S.) were assembled in an Argon-filled glove box (<0.1 ppm O_2 and H_2O , MBraun, Germany). The cell components were dried beforehand in a 70°C drying oven for at least 20 h. A gold wire micro-reference (core diameter of $50 \mu\text{m}$ and an additional $7 \mu\text{m}$ polyimide shrouding, Goodfellow Ltd., United Kingdom) is used as a reference electrode,¹⁷ placed in between two glass fiber separators (glass microfiber filter, 691, VWR, Germany) with a compressed thickness of $\sim 200 \mu\text{m}$ each. During cell assembly, $60 \mu\text{l}$ of LP57 electrolyte (1 M LiPF_6 in EC:EMC 3:7 w:w, <20 ppm H_2O , BASF, Germany) was added. The GWRE was lithiated with a constant current of 150 nA for 1 h and initially yielded a constant potential of 0.31 V vs. metallic lithium, which drifted toward the potential of an unlithiated gold wire within ca. 10 cycles (caused, we believe, by reaction of alloyed lithium with electrolyte oxidation products from the LNMO cathode at $4.9 \text{ V}_{\text{FC}}$ cell voltage). However, as shown in our previous work, artefact-free impedance spectra (indicated by the absence of inductive loops at low frequency; see Figure 3 in Reference 17) can be obtained from micro reference electrodes as long as the potential drift of the RE over the course of the impedance measurement is smaller than the chosen voltage amplitude. In the present work the potential drift of the RE over the course of the impedance measurement with a lower limit of 0.1 Hz is $\sim 3\text{--}4 \text{ mV}$, which is sufficiently below the perturbation amplitude during the EIS measurement (in this case 15 mV). This is verified by the absence of inductive loops at low frequency and was furthermore verified by comparing the impedance measurement with the micro-reference electrode with a standard EIS measurement using a symmetrical cell configuration (for the LNMO cathode; see Figure 6). It is emphasized that while the potential value of the reference electrode is unstable (i.e., it deviates from 0.31 V vs. metallic lithium after ~ 10 cycles), the reference electrode potential drift during the time period needed for an impedance measurement (~ 5 minutes) is still small ($<4 \text{ mV}$) compared to the potential perturbation. For details about the cell setup and the preparation of the gold wire, please refer to the original publication.¹⁷

The full-cells were cycled between 3.0 and 4.9 V cell voltage; for measurements with additional cells, the figure captions give the detailed experimental procedure (e.g., modified amplitudes or frequency ranges of impedance measurements). In the following, all potentials refer to the LNMO/graphite full cell voltage (indicated by the subscript FC) unless stated otherwise. Two formation cycles were carried out at 25°C at a C-Rate of C/10, while cycling was done at 40°C at a C-Rate of C/2. Potential-controlled impedance spectra (15 mV perturbation, from 100 kHz to 0.1 Hz ; acquisition time of 10 min./spectrum) were recorded during discharge at $4.4 \text{ V}_{\text{FC}}$ after a 1 h OCV (open-circuit voltage) phase as well as under blocking condition, which were achieved by fully delithiating the cathode by holding it at $4.9 \text{ V}_{\text{FC}}$ until

a current of $<C/40$ was obtained and then recording impedance spectra while holding the potential at $4.9 \text{ V}_{\text{FC}}$. Analogously, impedance spectra of the anode in blocking condition have been recorded by holding the potential at $3.0 \text{ V}_{\text{FC}}$ at the end of discharge (completely delithiated graphite) until a current of $<C/100$ is reached. The cycling protocol was carried out on a potentiostat (VMP 300, BioLogic, France). It should be noted that due to the relatively high impedance of the reference electrode, individual impedance spectra for anode and cathode cannot be obtained at frequencies above 100 kHz .

Results and Discussion

LNMO/graphite cycling data.—First we verified that the charge and discharge potentials are not affected by the OCV holds during discharge at $4.4 \text{ V}_{\text{FC}}$ and at the end of discharge/charge at $3.0 \text{ V}_{\text{FC}}$ / $4.9 \text{ V}_{\text{FC}}$, which were required for the EIS measurements. Figure 3 exemplarily shows three selected cycles at the beginning, the middle, and the end of the cycling procedure of the LNMO/graphite cell. The peak during discharge (red lines) is caused by the OCV phase and the subsequent impedance measurement, once the cell potential reaches $4.4 \text{ V}_{\text{FC}}$ (indicated by the black dashed line in Figure 3). From cycle 1 to 75 (at C/2 and 40°C), the capacity drops from $\sim 125 \text{ mAh}/\text{g}$ to $\sim 90 \text{ mAh}/\text{g}$ (compare also Figure 4), which is typical for LNMO/graphite cells, due to their high operating potential and instability at elevated temperatures.^{25,26} At the same time, the cell polarization increases, which can be seen easily when comparing the potential plateau around $4.65 \text{ V}_{\text{FC}}$ during charge (dark lines) and at approximately $4.55 \text{ V}_{\text{FC}}$ during discharge (green lines).

The discharge capacities and the coulombic efficiencies over all 85 charge/discharge cycles are shown in Figure 4 (formation cycles not shown). Discharge capacities slightly above $120 \text{ mAh}/\text{g}_{\text{LNMO}}$ ($\sim 16\%$ of the initial capacity are consumed by SEI formation during the first two cycles at C/10) are reached in the initial cycles, but owing to a rather poor coulombic efficiency which never reaches more than $\sim 99.3\%$ (see Figure 4), the initial capacity decreases by $\sim 30\%$ to $\sim 87 \text{ mAh}/\text{g}$ after only 85 cycles. This compares reasonably well with literature data on LNMO/graphite cells operated at 45°C at a sequence of C-rates (first ten cycles at C/10, followed by 40 cycles at C/4, and another 40 cycles by C/2), which lost $\sim 20\%$ of their initial capacity over the same number of cycles.²⁷ Our cycling data, capacity loss of $20\text{--}30 \text{ mAh}/\text{g}$ at a cycling rate of C/2 at 40°C , also agrees well with

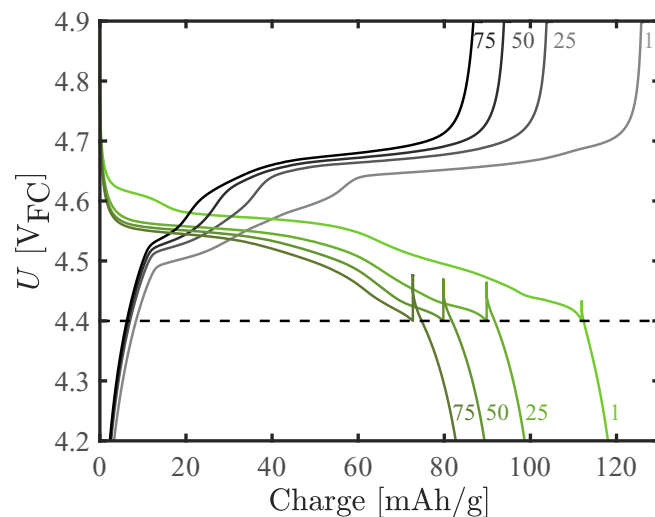


Figure 3. Exemplary charge (dark lines) and discharge (green lines) potential profiles for cycles 1, 25, 50, and 75 (marked in the figure) of the LNMO/graphite cell at 40°C , cycled at C/2 followed by a CV phase after charge until $I < C/40$ and a CV phase after discharge until $I < C/100$ between 3.0 and $4.9 \text{ V}_{\text{FC}}$. The peaks in the discharge curves are due to a 1 h OCV phase and a subsequent impedance measurement once the discharge potential reaches $4.4 \text{ V}_{\text{FC}}$.

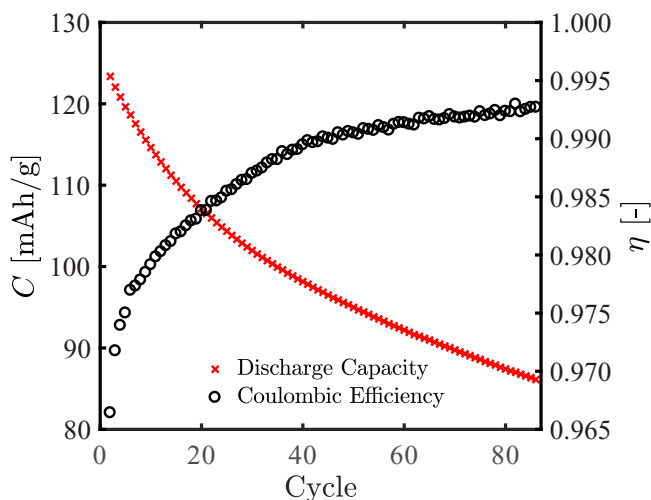


Figure 4. Discharge capacities for the LNMO/graphite cell cycled at 40°C and C/2 rate followed by a CCCV charge until $I < C/40$ and a CCCV discharge until $I < C/100$ in a potential window from 3.0 V_{FC} to 4.9 V_{FC} as well as the corresponding coulombic efficiencies.

the capacity loss of 30 mAh/g over 50 cycles at C/5 and 45°C, as reported by the group of Brett Lucht.²⁸ Thus, we conclude that the cycling data of the LNMO/graphite cells do not seem to be influenced significantly by the GWRE and the OCV periods required by for the EIS measurements. In the following we will focus our analysis to the impedance measurements performed during cycling of the cell.

Blocking conditions for the LNMO cathode in full-cells.—In the following, we will show that blocking conditions can indeed be achieved for the LNMO cathode in an LNMO/graphite full-cell by adding a constant voltage phase at the upper cutoff potential of 4.9 V_{FC} until the current decays below C/40, which leads to a condition where the cathode is fully delithiated so that the charge transfer resistance becomes very large (ideally, for perfect blocking conditions, R_{CT} would become infinitely large). For this purpose, an LNMO/graphite full-cell was built and charged galvanostatically at a C-Rate of C/10. Every 3 minutes during charge, the potential was held at its current value (no OCV phase), and an impedance spectrum with a perturbation of 50 mV was recorded in the frequency range from 100 kHz to 1 Hz (to obtain a short measurement time of ~2 min per spectrum). After reaching the upper cutoff potential of 4.9 V_{FC}, impedance spectra were recorded continuously (taking ~2 min each). Figure 5 demonstrates, how the cathode impedance spectra change upon approaching 100% SOC, showing exemplarily the EIS response at various potentials during the galvanostatic charge at potentials of 4.64 V_{FC}, 4.7 V_{FC}, 4.8 V_{FC}, and 4.9 V_{FC} as well as after increasingly long potential holds at the upper cutoff potential of 4.9 V_{FC}, after which EIS spectra are obtained potentiostatically while holding the potential. While the impedance spectra at 4.64 V_{FC} (blue line) resemble those simulated for non-blocking conditions (see blue line in Figure 2 between 100 kHz and 0.1 Hz), the impedance spectra after having held the cell potential at the upper cutoff potential approach those expected for blocking conditions, as is evident by comparing the red lines in Figure 5 with the red line in Figure 2.

To verify our above conclusions that the Nyquist plot of the cathode recorded in blocking conditions of an LNMO/graphite full-cell (i.e., after a 4.9 V_{FC} hold for 5 minutes) indeed follows the transmission line model for a blocking electrode, we prepared two additional cells, viz. one LNMO/graphite full-cell with GWRE and one LNMO/LNMO symmetric cell. The red data points in Figure 6 shows the impedance spectrum of the LNMO cathode of the LNMO/graphite full-cell, filled with the same electrolyte which was used for the cycling experiment (see Experimental), and subsequently charged at C/2 rate to 4.9 V_{FC}

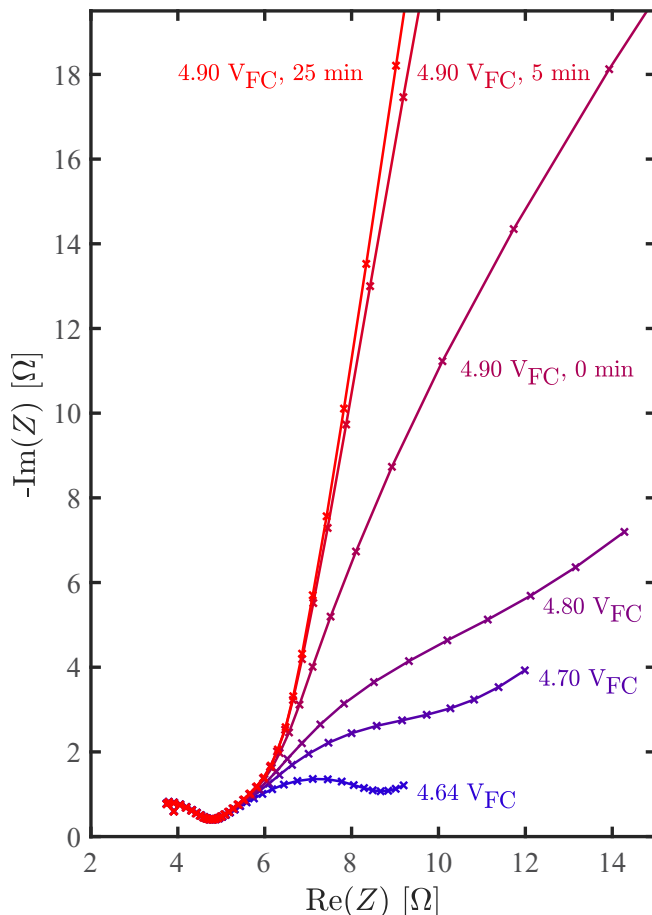


Figure 5. Evolution of the Nyquist plots of an LNMO cathode in an LNMO/graphite full-cell, obtained from EIS measurements (perturbation of 50 mV, 100 kHz–1 Hz) versus a GWRE. The data are recorded at a temperature of 25°C after two formation cycles at 25°C at C/10 followed by 5 C/10 cycles between 4.9 V_{FC} and 3.0 V_{FC}. Impedance spectra were obtained during galvanostatic charging of the cell at a charging rate of C/10 C and are shown from 4.64 V_{FC} up to 4.9 V_{FC}, followed by different holding times at 4.9 V_{FC}.

at 40°C and held at this potential for 5 minutes (after two formation cycles at 25°C and C/10), whereby the x- and y-axis values are multiplied by the conductivity of the electrolyte at the measurement temperature of 40°C ($\kappa = 11$ mS/cm). As can be seen in Figure 6 (red dashed line), the data can be fitted very well with a transmission line model without an $R_{Cont.}/Q_{Cont.}$ circuit element and with an infinitely large R_{CT} which is closely approached by a completely delithiated LNMO cathode. The resulting fit yields a value of 0.043 cm^{-1} for the product of $R_{Pore} \cdot \kappa$. In order to demonstrate that this approach yields reliable and meaningful physical-chemical parameters which describe ionic conductivity in the porous cathode electrode, a symmetric cell with two identical LNMO cathodes (albeit not cycled) and a non-intercalating electrolyte (10 mM TBAClO₄ in EC:EMC 3:7 w:w) was built. Its impedance response is shown by the black data in Figure 6 whereby it should be noted that the symmetric cell impedance was divided by two, as it represents the sum of two identical electrodes. The transmission line model for blocking conditions yields a very good fit of the data (see dashed black line) and a value of 0.033 cm^{-1} for $R_{Pore} \cdot \kappa$.

While the impedance spectra from both the LNMO cathode in the LNMO/graphite full-cell (measured with the GWRE) and from the LNMO/LNMO symmetric cell nicely fit the transmission line model for a blocking electrode, it remains to be determined whether the same pore resistance characteristics are observed for both nominally identical cathodes for these two different measurement

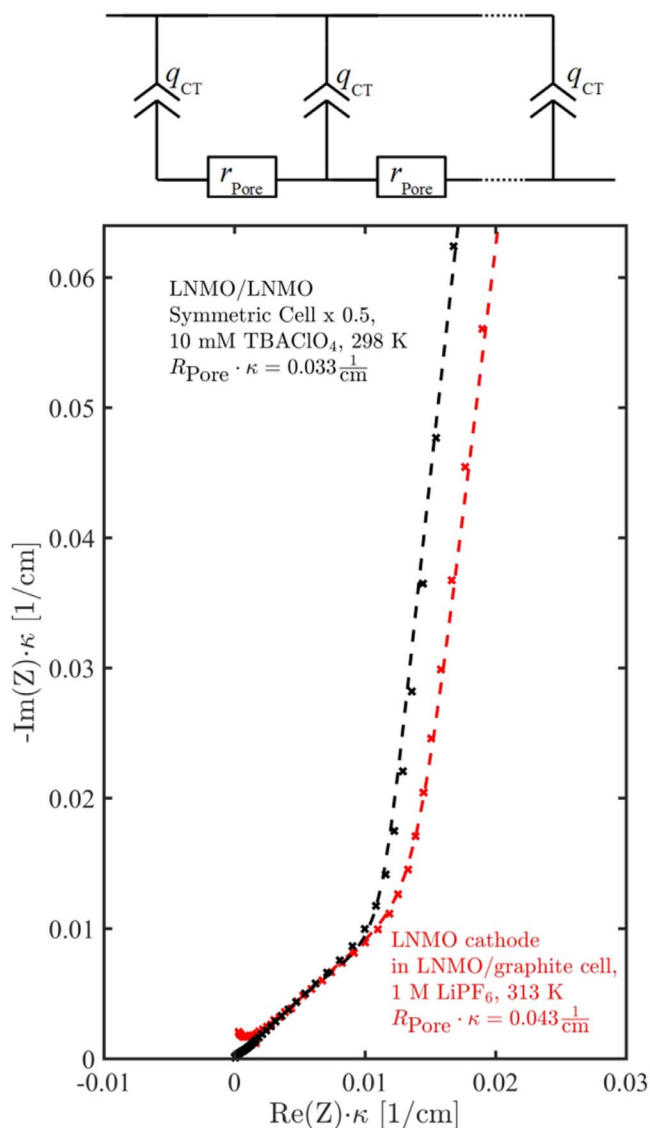


Figure 6. Comparison of the conductivity-scaled Nyquist spectra (i.e., real and imaginary impedances multiplied by the ionic conductivity) of an LNMO cathode in an LNMO/graphite cell (with GWRE) in blocking conditions (red data points) versus an LNMO/LNMO symmetric cell with non-intercalating electrolyte (black data points), whereby the latter impedance spectrum was divided by two in order to obtain the response of one LNMO cathode. The latter was measured after 12 h wetting by a non-intercalating electrolyte (10 mM TBAClO₄ in EC:EMC 3:7 w:w) at 25°C and using one CG2500 separator; the conductivity of this electrolyte at 25°C was determined to be $\kappa = 0.332$ mS/cm. The LNMO cathode impedance spectrum was obtained at 40°C after C/2 charging to 4.9 V_{FC} and holding that potential for 5 min (after two formation cycles); the electrolyte was 1 M LiPF₆ in EC:EMC (3:7, w:w) and had a conductivity at 40°C of $\kappa = 11$ mS/cm. Impedance spectra were recorded in the frequency range from 100 kHz to 0.1 Hz using an excitation amplitude of 15 mV and 20 mV for the LNMO/graphite cell and the symmetric cell, respectively. Both spectra were shifted to the origin for better comparability. The fit of the data to a simple transmission line model (shown in the figure) is represented by the dashed line and the resulting values of $R_{\text{Pore}} \cdot \kappa$ are given in the figure.

approaches. This can be checked by determining the corresponding MacMullin numbers (N_M), which would have to be the same for the nominally identical LNMO cathodes (i.e., having the same porosity (ϵ) and the same tortuosity (τ) measured in the two different cell configurations:

$$N_M = \frac{\tau}{\epsilon} = R_{\text{Pore}} \cdot \kappa \cdot \frac{A}{d} \quad [13]$$

where A is the area of the electrodes ($A = 0.95$ cm²) and d is their thickness ($d = 58$ μm). The resulting MacMullin numbers obtained from the analysis of the data in Figure 6 are 7.0 ± 0.3 for the LNMO cathode measured in the LNMO/graphite full-cell with the GWRE under blocking conditions and 5.4 ± 0.3 for the nominally identical LNMO cathode measured in the LNMO/LNMO symmetric cell configuration, whereby the error results from the limited accuracy of the coating thickness measurement (± 2 μm). More important than the measurement error for a given cell is the cell-to-cell variation (due minor differences in cell assembly and/or LNMO electrode coating), which was estimated by analyzing three more LNMO/LNMO symmetric cells and two more LNMO/graphite cells with GWRE (data not shown), yielding overall mean MacMullin numbers of 6.3 ± 0.6 for the LNMO electrodes measured in the LNMO/graphite full-cell setup (based on 3 repeat experiments) and 5.9 ± 0.6 for the LNMO cathode in the LNMO/LNMO symmetric cell setup (based on 4 repeat experiments). Thus, within the experimental error represented by the above standard deviations, both methods yield identical values for the MacMullin number. The fact that these values for the here used LNMO cathode with 5%wt conductive carbon are substantially lower than those we reported previously for an LNMO cathode with 2%wt conductive carbon ($N_M \approx 17$)¹⁹ is simply related to the substantial lowering of the MacMullin number as the conductive carbon content is being increased (e.g., for lithium iron phosphate cathodes with comparable porosity, the MacMullin number decreases from 21 to 12 when the carbon content is increased from 5% to 15% wt.¹⁹). In summary, the above analysis demonstrates that blocking conditions are reached for an LNMO/graphite full-cell by holding the cell potential at 4.9 V_{FC} (Figure 5), and that reliable values for the ionic conduction characteristics of the LNMO cathode (i.e., its MacMullin number) can be obtained under these conditions via a simple transmission line model (Figure 6). In the following, we will now analyze the evolution of the impedance spectra over extended charge/discharge cycles and will utilize impedance measurements under blocking and non-blocking conditions in order to quantify the contributions derived from R_{Pore} , R_{Cont} , and $R_{\text{CT-non-blocking}}$.

LNMO cathode impedance evolution in LNMO/graphite cells.—

The cycle dependent Nyquist plots for the cathode in non-blocking condition at 4.4 V_{FC} and in blocking condition (i.e., after a potential hold at 4.9 V_{FC} until $I < C/40$) are summarized in Figure 7 for every 25th cycle.

At the highest frequencies, a semi-circle can be observed, both, in non-blocking (Figure 7a) and in blocking conditions (Figure 7b), which is identical in magnitude and independent of the SOC and is thus ascribed to the contact resistance (R_{Cont} , region II in Figure 1 and Figure 2). Over the course of charge/discharge cycling, this contact resistance clearly increases, evidenced by a shift of the spectra to larger real resistance values. It must be noted, however, that it is difficult to directly assess the value of the contact resistance, since in the experimentally accessible frequency range (100 kHz to 0.1 Hz; see Experimental section), only part of the contact resistance semi-circle can be obtained (this is illustrated by the modelled impedance response shown in Figure 2, where the 100 kHz data point is marked by the third yellow cross from the left). Therefore, the diameter of the semi-circle corresponding to the contact resistance cannot be determined visually from the acquired spectra without knowing the value of the high frequency resistance (R_{HFR} , region I in Figures 1 and 2). In non-blocking conditions (Figure 7a) the contact resistance semi-circle is followed by another distorted semi-circle, which increases in diameter from initially ≈ 1.5 Ω to 2 Ω in cycle 75, while at the lowest frequencies a Warburg type behavior can be observed (W , region IV in Figures 1 and 2). On the other hand, in blocking conditions (Figure 7b), an essentially straight line can be observed at medium frequencies (with an angle of close to 45 degrees in the first cycle), gradually turning into a nearly vertical line at the lowest frequencies, as one would expect for blocking conditions (compare the red line in region III marked in Figure 2). Thus, holding the cell potential at 4.9 V_{FC} does lead to the very large charge transfer resistance (R_{CT}) which is required to closely

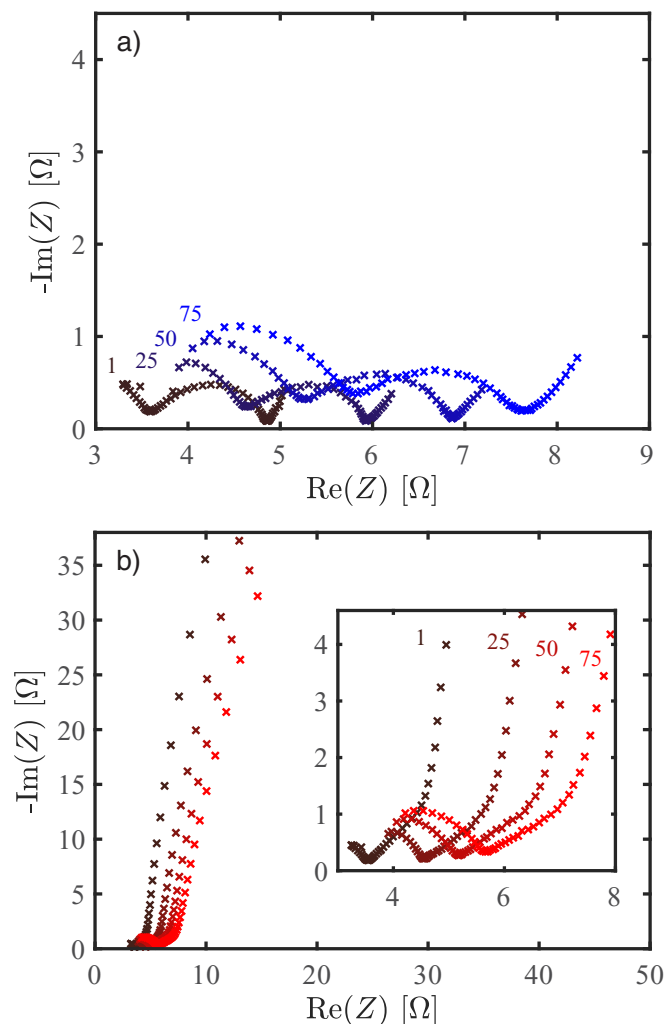


Figure 7. Evolution of the impedance spectra of the LNMO cathode (every 25th cycle; cycle numbers 1, 25, 50 and 75 are marked in the figure) during cycling of an LNMO/graphite cell at a rate of C/2 at 40°C: a) at 4.4 V_{FC} under non-blocking conditions (recorded at OCV after a 1 h OCV period); b) after potential hold at 4.9 V_{FC} under blocking conditions (recorded at a controlled potential of 4.9 V after a potential hold at 4.9 V until the current was below C/40). Potential-controlled EIS spectra were recorded with an amplitude of 15 mV in the frequency range from 100 kHz to 0.1 Hz.

approach blocking conditions. The decrease of the angle in the mid frequency region (initially close to 45 degrees) with cycling could be caused by electrolyte degradation products deposited in the cathode pores (see discussion after Figure 9), which change the pore structure inside the cathode.

In the following, the measured spectra of the half-cell cathode impedances are analyzed using Matlab (v. 2016b). Minimization of the sum of squares using a modulus weighing according to Lasia²⁰ was performed using Matlab's *fminsearch*²⁹ algorithm, and 95% confidence intervals are calculated via the Jacobian matrix obtained with the *jacobianest*³⁰ function. For each charge/discharge cycle, spectra in non-blocking condition at 4.4 V_{FC} and in blocking condition are fitted simultaneously using the equivalent circuit model shown in Figure 1. For the fitting of the spectrum in non-blocking conditions, 10 fitting parameters are required (viz., R_{HFR} , R_{Cont} , Q_{Cont} , α_{Cont} , R_{Pore} , R_{El} , $R_{CT-non-blocking}$, Q_{CT} , α_{CT} , and W). In blocking conditions, the numerically identical parameters are used, except that a different value for the charge transfer resistance, referred to as $R_{CT-blocking}$ (in contrast to $R_{CT-non-blocking}$) is fitted and that the Warburg element is omitted. In summary the spectrum in non-blocking condition requires

ten and the spectrum in blocking condition nine fitting parameters for an accurate description of the equivalent circuit model in Figure 1. However, since it is reasonable to assume that changes in the properties of the electrode and the active material are negligible within a single charge/discharge cycle, most of the parameters used to fit the blocking and non-blocking spectra within a given cycle are identical (viz., R_{HFR} , R_{Cont} , Q_{Cont} , α_{Cont} , R_{Pore} , R_{El} , Q_{CT} , and α_{CT}), so that only eleven parameters are required to fit both spectra for a given cycle (see Table I).

Seeking to reduce the number of the free parameters in order to increase the accuracy of the fitted parameters, the following simplifications can be made. One is based on the assumption that the electronic resistance within the electrode (R_{El} in Figure 1) is small compared to the ionic resistance in the electrode and that its value does not change significantly over the course of the cycling experiment (to a good approximation, it would be sufficient that the ratio of R_{Pore}/R_{El} remains at $\gg 1$). The maximum value of R_{El} for our pristine LNMO cathodes was obtained by a 2-point probe measurement, placing the LNMO electrode between two copper blocks, each equipped with a current and voltage lead (at a compression of 0.1 MPa using a static material testing machine zwickiLine from ZwickRoell, Ulm, Germany) and using a nanovoltmeter (Keithley 2182) in combination with a DC current source (Keithley 6221). This yielded a value of $R_{El} \approx 0.1 \Omega$, (≈ 30 -fold lower than R_{Pore} , as will be shown later), so that $R_{El} = 0.1 \Omega$ was used as a fixed and constant resistance in the fitting of all impedance spectra. The other simplification in fitting the impedance spectra is related to the high-frequency resistance (R_{HFR} in Figure 1). While theoretically its value could be obtained from the overall fit of the impedance spectra, it would decrease the quality of the fit, because only a fraction of the contact resistance semi-circle can be observed with the experimentally accessible upper frequency limit of 100 kHz for the GWRE (see Figure 1 and Figure 7). The pure high-frequency resistance for the LNMO/graphite full-cell ($R_{HFR,full-cell}$), however, could be determined by measuring the *full-cell* impedance between anode and cathode after the cycling test, as in this case an upper frequency limit of 7 MHz could be used, so that despite the LNMO contact resistance the high-frequency real axis intercept can be obtained. This yielded a value of $R_{HFR,full-cell} = 4.8 \Omega$, i.e., of 2.4 Ω for each half-cell. In addition, analysis of the graphite impedance data using the GWRE in the same setup (the detailed analysis of the anode data will be submitted soon), where the high frequency resistance even at an upper frequency limit of 100 kHz can be determined unambiguously, yielding a *cycle independent* value of $R_{HFR,anode} = 2.4 \Omega$. As the GWRE sits in the center of two glass fiber separators, the high frequency resistance of the anode and the cathode half-cells are identical.¹⁷ From this it can be concluded that the high frequency resistance (R_{HFR} in Figure 1), i.e., the resistance caused by the ionic resistance in the separator of the LNMO half-cell, remains essentially constant at a value of 2.4 Ω . Therefore, the value of R_{HFR} in the following impedance fits was kept constant at 2.4 Ω , reducing the number of final fitting parameters to nine (viz., R_{Cont} , Q_{Cont} , α_{Cont} , R_{Pore} , $R_{CT-non-blocking}$, $R_{CT-blocking}$, Q_{CT} , α_{CT} , and W), which are fitted simultaneously to each of the two impedance spectra (blocking and non-blocking conditions) per cycle.

Exemplary fits of the cathode impedance spectra of the LNMO/graphite full-cell after 30 cycles both in blocking condition (potential hold at 4.9 V_{FC}) and in non-blocking condition at 4.4 V_{FC} are shown in Figure 8. The fitted impedance spectra (lines in Figure 8) with the above listed set of 9 fitting parameters provide quite a good fit to the impedance data (black crosses) under both conditions over the entire frequency range (100 kHz to 0.1 Hz).

Figure 9 collects the values of the most relevant equivalent circuit model parameters for the LNMO cathode and depicts their evolution with cycling as well as their 95% confidence intervals. As discussed above, the high frequency resistance (R_{HFR}) and the electronic resistance (R_{El}) are kept constant to allow for an explicit determination of the contact resistance. The contact resistance is found to increase from $\approx 1 \Omega$ initially to $\approx 3 \Omega$ after 85 cycles at C/2 at 40°C (yellow symbols in Figure 9a), which confirms the observation made in the discussion

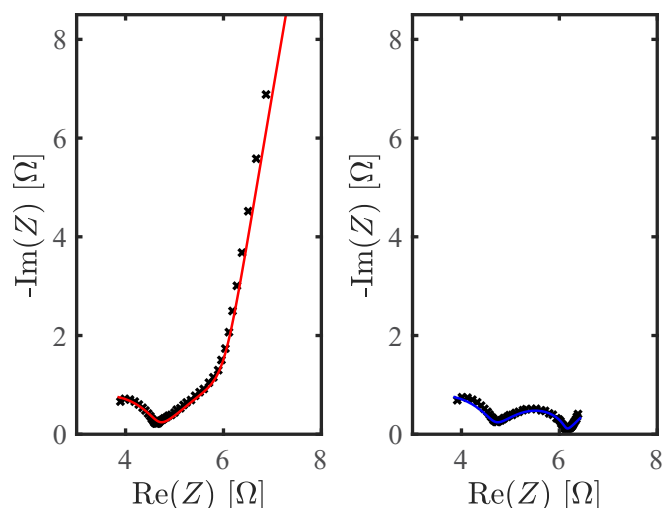


Figure 8. Exemplary fits (shown as solid lines) of the cathode impedance at cycle 30 obtained from the LNMO/graphite full-cell in blocking condition at 4.9 V_{FC} (left) and non-blocking conditions at 4.4 V_{FC} (right). Both spectra are fitted simultaneously, using the equivalent circuit model shown in Figure 1 with the same values for most parameters ($R_{\text{Cont.}}$, $Q_{\text{Cont.}}$, $\alpha_{\text{Cont.}}$, R_{Pore} , Q_{CT} , α_{CT}) and individual values for the charge transfer resistance in blocking condition ($R_{\text{CT-blocking}}$), the charge transfer resistance in non-blocking condition at 4.4 V_{FC} ($R_{\text{CT-non-blocking}}$), and the Warburg diffusion element (W) which is only used in non-blocking condition. AC impedance data (black crosses) were recorded at 40°C between 100 kHz and 0.1 Hz (15 mV voltage perturbation) after holding the cell potential at 4.9 V_{FC} (blocking condition, left) or at 4.4 V_{FC} after an 1 h OCV period (non-blocking condition, right).

of Figure 7, namely that the shift of the spectra to higher real resistance values is due to an increase of the high-frequency semi-circle representing the contact resistance. This increase of the LNMO cathode's contact resistance fits very well to the observation that a delamination of the LNMO electrode from the current collector occurs during cycling at elevated temperatures (60°C),³¹ the underlying mechanism of which will be a subject of a future work.³² Compared to the contact resistance, the pore resistance (R_{Pore} , green symbols) increases from an initial value of $\approx 3.5 \Omega$ to $\approx 5 \Omega$ after 85 cycles, while the charge transfer resistance at 4.4 V_{FC} ($R_{\text{CT-non-blocking}}$, purple symbols) starts at $\approx 0.5 \Omega$ and increases to only $\approx 0.7 \Omega$ after 85 cycles. Thus, the contact resistance shows the strongest increase over the 85 charge/discharge cycles of +300%, while the pore and charge transfer resistance at 4.4 V only increase by $\approx 45\%$ and $\approx 30\%$, respectively (see Figure 9b). The charge transfer resistances in blocking-condition (not shown in Figure 9) is found to be $\approx 900 \Omega$, a very large value compared to the other resistances, as would be expected for the observed blocking electrode behavior, i.e., the nearly vertical line at lowest frequencies (see Figure 7b or the left panel of Figure 8). The error bars of all resistances shown in Figure 9 are mostly smaller than 25%, which is quite reasonable considering that two spectra were fitted simultaneously with a restricted parameter set for any given cycle, thus suggesting that the equivalent circuit representation of the LNMO cathode in Figure 1 captures most of the relevant processes. The irregularities observed for the fitted contact and pore resistance around cycles five to fifteen can be explained with the drift of the GWRE potential from its lithiated state to its unlithiated potential (see Experimental).

Over the course of the 85 charge/discharge cycles at 40°C, the overall resistance of the LNMO cathode ($R_{\text{Cont.}} + f(R_{\text{Pore}}, R_{\text{CT-non-blocking}})$) increases from an initial value of $\approx 5 \Omega$ to $\approx 9 \Omega$ (see Figure 9a). At the given charge/discharge current of $\approx 1 \text{ mA}$ (based on a capacity of $\approx 2 \text{ mAh}$ and a rate of C/2), this would predict an increase in cathode polarization of only $\approx 4 \text{ mV}$ and would thus be rather negligible. As can be seen from the cell voltage vs. capacity data in Figure 3, the increase in the polarization of the LNMO/graphite cell seems to be

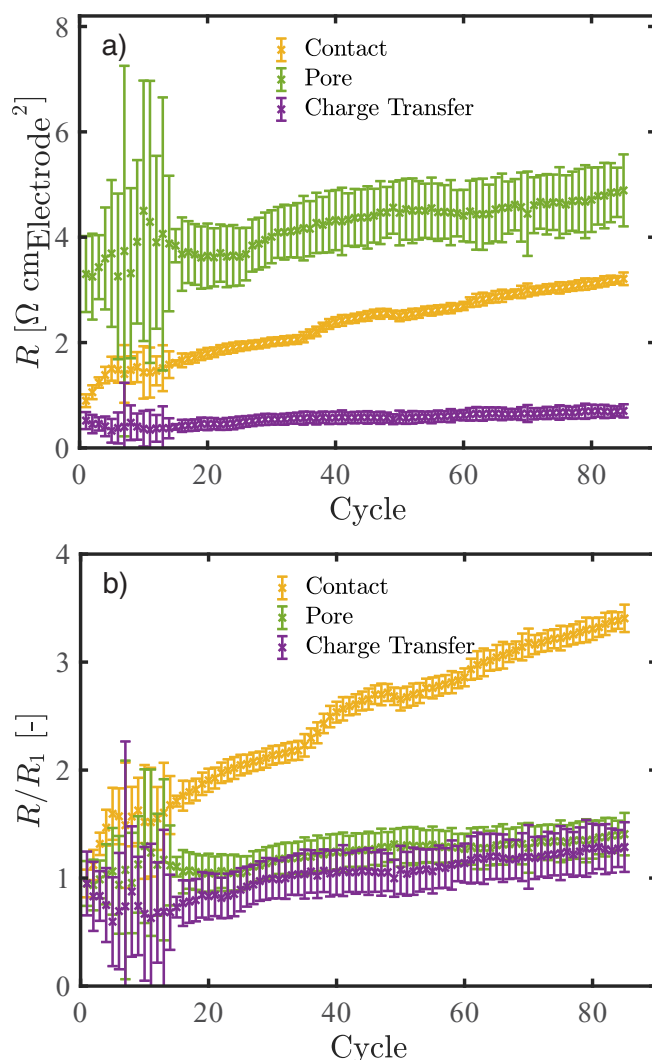


Figure 9. a) Evolution of the contact resistance ($R_{\text{Cont.}}$), the charge transfer resistance at 4.4 V_{FC} ($R_{\text{CT-non-blocking}}$, obtained under non-blocking conditions), and the pore resistance (R_{Pore} , obtained under blocking conditions) of the LNMO cathode, normalized to the electrode area, in the LNMO/graphite full-cell over extended charge/discharge cycling at 40°C at a rate of C/2 between 3.0 and 4.9 V_{FC} (the corresponding capacity vs. time plot and exemplary voltage vs. capacity plots are shown in Figure 4 and Figure 3, respectively; the formation cycles are not included). The shown values were determined by simultaneously fitting two impedance spectra per cycle, one in blocking condition and one in non-blocking condition as shown in Figure 8. The high frequency resistance contribution to the cathode (R_{HFR} in Figure 1) was set to a constant value of 2.4Ω , and the electronic resistance in the cathode (R_{El} in Figure 1) was set to 0.1Ω (see discussion in the text). b) Resistances normalized to their initial value after formation. Error bars indicate the parameters' 95% confidence interval from the fit.

much larger than 4 mV, which is due to the fact that the largest contribution to the cell polarization with cycling is caused by a substantial gain in the impedance of the anode (this analysis will be subject of a future publication).

Using the charge transfer resistances at 4.4 V of $\approx 0.5\text{--}0.7 \Omega$ (see purple lines in Figure 9a), the linearized Butler-Volmer equation allows to estimate the exchange current density:

$$i_0 = \frac{RT}{F} \cdot \frac{1}{A_{\text{LNMO}} \cdot R_{\text{CT-non-blocking}}} \quad [14]$$

with R , T , and F being the gas constant (8.831 kJ/mol K), temperature (303 K), and the Faraday constant (96485 As/mol),

respectively. In addition, A_{LNMO} represents the active surface area of the LNMO, which can be estimated using the mass of LNMO (13.7 mg) in the cell and its BET surface area (0.9 m²/g), equating to $A_{\text{LNMO}} = 123 \text{ cm}^2_{\text{LNMO}}$. Based on this, we find an exchange current density of 0.43–0.30 mA/cm²_{LNMO} at 4.4 V_{FC} (i.e., at ≈ 7 –12% SOC, s. Figure 3), which is within the range of exchange current densities for intercalation materials reported in the literature (0.02–0.3 mA/cm²_{LNMO} for LNMO,³³ 0.17 mA/cm²_{LFP} for LiFePO₄,³⁴ and 2.5 mA/cm²_{Graphite} for graphite³⁵).

The observed increase in the pore resistance with cycling (see green lines in Figure 9) can be explained by a decrease of the effective electrolyte conductivity in the pores, likely caused by a partial blockage of the cathodes' pore volume by electrolyte oxidation fragments, thereby decreasing the cathode's void volume, which would probably also be accompanied by an increase in the cathode's tortuosity. In the literature, it is reported that the electrode/electrolyte interface at the LNMO cathode (often referred to as CEI) is not stable, compared to the solid electrolyte interface (SEI) on the graphite anode, so that electrolyte oxidation would happen at the surface of the LNMO particles.^{2,25,26} This is consistent with the observation that both, charge transfer resistance at 4.4 V and the pore resistance, increase over the 85 charge/discharge cycle by 30% and 45% respectively.

The feasibility of the obtained fitting parameters for the impedance spectra can also be checked by examining the values the fit yielded for the capacitive constant phase elements related to both the LNMO cathode material (Q_{CT} , see Figure 1) and the contact resistance ($Q_{\text{Cont.}}$, see Figure 1). A rough order of magnitude estimate of the capacitances can be done by neglecting the constant phase factor, yielding values of $Q_{\text{Cont.}} \approx 10 \text{ } \mu\text{F}$ and $Q_{\text{CT}} \approx 1 \text{ mF}$. If normalized to the exposed areas of the current collector/electrode interface ($\approx 1 \text{ cm}^2$) and the LNMO area ($A_{\text{LNMO}} = 123 \text{ cm}^2_{\text{LNMO}}$), the resulting area specific capacitance amounts to $\approx 10 \text{ } \mu\text{F}/\text{cm}^2_{\text{surface}}$ in either case, which is a reasonable value for the double layer capacitance.

The results obtained from this study suggest that the charge transfer resistance of the LNMO cathode is not increasing substantially during extended charge/discharge cycling, which is in disagreement with reports in the literature. For example, Aurbach et al. analyzed the impedance of LNMO/graphite cells by measuring the impedance of the LNMO electrode versus a lithium wire reference electrode, showing that the impedance in the high-to-medium frequency range increases during cycling, which they ascribed to an increase of a combination of a surface film (inferred from an increase in the LiF surface coverage measured by XPS) and a charge transfer resistance at the LNMO/electrolyte interface.²⁶ However, examining the semi-circle at high-to-medium frequencies in their measurements (apex-frequency = 1.58 kHz, $R_{\text{semi-circle}} = 126 \text{ } \Omega$), one obtains a capacitance value of $\approx 1 \text{ } \mu\text{F}$, which is more consistent with a contact resistance between the LNMO cathode and the current collector rather than with the capacitance of the high surface area of the porous LNMO cathode. This suggests that their reported increase in LNMO surface/charge transfer resistance is likely incorrect and that the impedance increase in their study is probably due to an increase in $R_{\text{Cont.}}$, analogous to what is shown in Figure 9. Similarly, Lu et al. analyzed the impedance of LNMO/graphite cells (full-cell impedance) and claimed that the observed increase of the high frequency semi-circle is related to an increase in the thickness of a resistive film on the LNMO surface.²⁵ In summary, these studies claim the formation of a resistive film and/or an increase in the charge transfer resistance during extended cycling of an LNMO cathode, contrary to our analysis shown in Figure 9, which we believe is due to an incorrect assignment of the impedance data, caused primarily by the interference from contact and/or pore resistances with the charge transfer resistance. Here it may be noted that similarly incorrect assignments were discussed previously for LFP/graphite electrodes by Gaberscek et al.³⁶

By exemplary analysis of LNMO half-cell data we have demonstrated that it is possible to analyze the impedance of an LNMO cathode in an LNMO/graphite full-cell with a GWRE in both blocking and in non-blocking conditions over the course of cycling, which

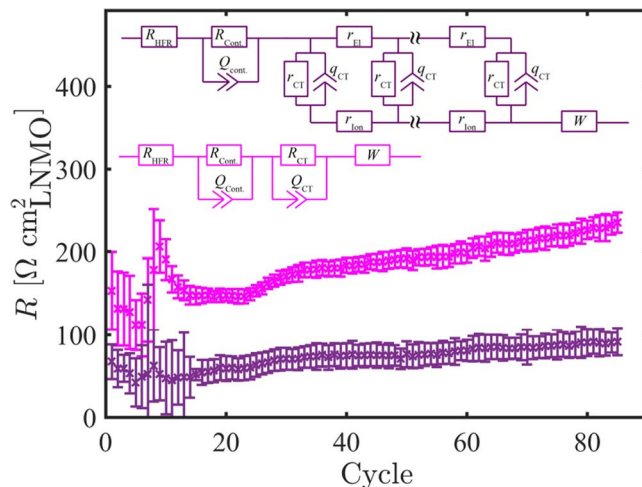


Figure 10. Comparison of the areal charge transfer resistances, normalized to the LNMO BET surface area (123 cm²), obtained from the transmission line model including pore resistance (lilac) with the *apparent* charge transfer resistance extracted from the conventionally used simplified equivalent circuit (magenta) with one R/Q element to describe the mid frequency region (region III in Figure 1 and Figure 2), while one R/Q element is used to describe the high-frequency region semi-circle (region II in Figure 1 and Figure 2).

in turn allows for an unambiguous determination of all parameters in the general transmission line model with small errors. The obtained resistances are found to be of reasonable magnitude and in good agreement with the literature and can be monitored in-situ over the course of extended cell cycling. This minimizes the required number of cells compared to the rather cumbersome conventional approach, in which pairs of cells are cycled to a certain number of cycles and the impedances of the half-cells are obtained after cell disassembly and reassembly of anodes and cathodes into symmetric cells—clearly advantageous from an experimental point of view. Furthermore, in most impedance studies in the literature, the observed distorted semi-circle of the impedance spectra in non-blocking condition (compare Figure 7a) are fitted and interpreted in terms of a single R/Q equivalent circuit element in the mid frequency region, yielding an apparent charge transfer resistance,^{10,26,37} even though this frequency region also contains the pore resistance (region III in Figure 1 and Figure 2). To highlight the difference in the charge transfer resistance values obtained by these two approaches, we compare the charge transfer resistance obtained from our simultaneous fit in blocking and non-blocking conditions (see data in Figure 9, fitted to the equivalent circuit shown in Figure 1) with the apparent charge transfer resistance obtained when the distorted semi-circle (see Figure 7a, second semi-circle from the left) is simply fitted with an R/Q element (i.e., using the conventionally applied simplified equivalent circuit depicted in Figure 10 (magenta)). The two different equivalent circuit models are depicted together with the resulting charge transfer resistances (including 95% confidence intervals) in Figure 10.

Figure 10 (magenta symbols) illustrates the stark overestimation of the apparent charge transfer resistance using the simplified equivalent circuit model, which neglects the ionic resistance within the porous electrode: the obtained apparent charge transfer resistance larger by a factor of two to three (magenta symbols) compared to the charge transfer resistance obtained from our transmission line model evaluated simultaneously in blocking and non-blocking conditions (lilac symbols), which is due to the fact that in the former approach the pore resistance (R_{pore}) is added erroneously to the charge transfer resistance. Thus, in our opinion, the simplified equivalent circuit model is a coarse oversimplification for a porous electrode, and the true charge transfer resistance constitutes only a fraction of the observed mid-frequency semi-circle width.

Conclusions

We utilize a gold wire micro-reference electrode to separate anode and cathode spectra in an LNMO/graphite full-cell over the course of extended charge/discharge cycling. The LNMO cathode impedance spectra could be deconvoluted into individual resistance contributions by measuring in non-blocking conditions at 4.4 V_{FC} and in blocking conditions by holding the LNMO/graphite full-cell potential at 4.9 V_{FC}. This novel impedance analysis approach, i.e., the simultaneous fitting of impedance spectra measured in blocking and non-blocking condition, enables the in-situ quantification of the cycle dependent charge transfer, contact, and pore resistances, over the course of extended charge/discharge cycling, which is a powerful analysis tool for aging studies. We applied our approach exemplarily to an LNMO cathode, but generally the technique could also be applied to other active materials which can be brought into a blocking condition in a full-cell configuration, such as, e.g., lithium iron phosphate, graphite, or LTO.

Acknowledgment

J. L. gratefully acknowledges the funding by the Bavarian Ministry of Economic Affairs and Media, Energy, and Technology for its financial support under the auspices of the EEBatt project. D. P. acknowledges funding from BASF SE within the framework of the Network on Electrochemistry and Batteries. The authors thank Werner Strunz from Zahner for his helpful remarks regarding the general transmission line model and Andrzej Lasia for his comments on proper weighing of impedance spectra and his critical feedback on the equivalent circuit model.

Appendix

Diffusion impedances of solid diffusion and liquid diffusion.—As outlined in the Theory section, the imaginary part of the impedance of a diffusion process depends on the diffusion coefficient of the diffusing species as well as the cross sectional area, bulk concentration of the species in the medium, and the temperature. The diffusion coefficient of lithium in the liquid electrolyte is on the order of 10^{−10} m²/s for typical lithium ion battery electrolytes at room temperature.³⁸ For the solid state diffusion coefficient, the range of reported diffusion coefficients in various cathode materials range from 10^{−12} m²/s to 10^{−19} m²/s.³⁹ Mohamedi et al. report an apparent solid state diffusion coefficient for LNMO of 10^{−14} m²/s to 10^{−16} m²/s.³³ In the following, we will present our own conservative estimate of the lower limit for the solid state diffusion coefficient of lithium in LNMO (for even larger solid state diffusion coefficients, the impact of the solid state diffusion on the impedance spectrum would be reduced further).

LNMO electrodes with a very small loading of 10 μg/cm² were cycled at 25 °C versus metallic lithium in a three electrode configuration with a lithium reference electrode in the potential range from 3 V to 4.9 V vs. lithium using a standard electrolyte (LiPF₆ in EC:EMC 3:7, w:w) and two glass fiber separators. The LNMO was always deintercalated (charged) at a constant current of C/3 until the cutoff of 4.9 V vs. the lithium RE was reached. Constant current intercalation (discharge) was done at C-Rates from 1C to 500C until the lower cutoff potential of 3.0 V vs. lithium was reached. By minimizing the loading, the total current in the cell is small (at 500C, *I* = 5 mA) and all overpotentials from separator resistances, contact resistances, and the concentration gradients in the liquid electrolyte play an insignificant role. The intercalation direction was chosen on purpose to allow large overpotentials. In these measurements, ~20% of the full (1C) capacity could be extracted from the low loaded LNMO cathodes at a C-Rate of 100C. Assuming, conservatively, that all limitations in this experiment are a result of the solid state diffusion inside the active material particles (s. above), i.e., neglecting all other resistances and/or a concentration buildup in the liquid phase, we can now estimate the lower limit of the solid state diffusion coefficient. 20% of the capacity of the LNMO particles (15 μm diameter, based on SEM images) can be extracted from the particle shell region between *r* = 7.0 μm to *r* = 7.5 μm (corresponding to 20% of the particle volume). During 20% of the time of a 100C intercalation (*t* = 0.2 · 36s = 7.2 s), the lithium in the LNMO has to travel at least Δ*r* = 0.5 μm, equating to an estimated diffusion coefficient of $D = \Delta r^2 / t = 3.5 \cdot 10^{-14} \frac{\text{m}^2}{\text{s}}$.

With the above estimates for the solid and the liquid diffusion coefficient,³⁸ the diffusion impedance can be estimated (strictly valid only for semi-infinite diffusion inside a film) with Equation 12 and the definition of the Warburg coefficient (compare Reference 40, Eq. 5–40 for the same kinetic rate constants for forward and backward reaction $k_f = k_b$)

$$W = \frac{4 \cdot RT}{z^2 F^2 A C \sqrt{2 \cdot D}} \quad [\text{A1}]$$

The Warburg coefficient of the liquid electrolyte phase at a frequency of 0.1 Hz thus yields a value of

$$W_{\text{Liquid}} = \frac{4 \cdot RT}{z^2 F^2 \cdot 0.95 \text{ cm}^2 \cdot 1000 \frac{\text{mol}}{\text{m}^3} \sqrt{2 \cdot 10^{-10} \frac{\text{m}^2}{\text{s}}}} = 792 \frac{\text{m}\Omega}{\sqrt{\text{s}}} \quad [\text{A2}]$$

while for solid state diffusion the Warburg coefficient at a frequency of 0.1 Hz can be estimated as

$$W_{\text{Solid-state}} = \frac{4 \cdot RT}{z^2 F^2 \cdot 123 \text{ cm}^2 \cdot 10700 \frac{\text{mol}}{\text{m}^3} \sqrt{2 \cdot 3.5 \cdot 10^{-14} \frac{\text{m}^2}{\text{s}}}} = 31 \frac{\text{m}\Omega}{\sqrt{\text{s}}} \quad [\text{A3}]$$

Here, the lithium concentration in the solid (10700 mole/m³) is calculated for an LNMO particle at 50% SOC ($\equiv 70 \text{ mAh/g}_{\text{LNMO}} = 252 \text{ As/g}_{\text{LNMO}}$), using a bulk density of 4.4 g/cm³ ($252 \text{ As/g} \cdot 4.4 \text{ g/cm}^3 / 96485 \text{ As/mol} \cdot 10^6 \text{ cm}^3/\text{m}^3 = 10700 \text{ mol/m}^3$). With the above Warburg coefficients, Warburg impedances of $Z_{\text{W}}^{\text{Liquid}}$ (0.1 Hz) = 1 Ω and $Z_{\text{W}}^{\text{Solid-state}}$ (0.1 Hz) = 39 mΩ are obtained. This means that the contribution of the solid state diffusion impedance at the lowest frequency measured in this work (0.1 Hz) is 1.5 orders of magnitude smaller than the diffusion impedance caused by the liquid electrolyte. Based on this result, the solid state diffusion inside the active material is negligible, i.e., we can omit the Warburg element in series to the charge transfer resistance in the equivalent circuit model in Figure 1, but must place a Warburg element in series to the separator resistance to capture the effect of liquid diffusion.

References

- K. Xu, *J. Electrochem. Soc.*, **154**, S9 (2007).
- S. R. Li, C. H. Chen, X. Xia, and J. R. Dahn, *J. Electrochem. Soc.*, **160**, A1524 (2013).
- T. R. Jow, M. B. Marx, and J. L. Allen, *J. Electrochem. Soc.*, **159**, A604 (2012).
- J. P. Schmidt, T. Chrobak, M. Ender, J. Illig, D. Klotz, and E. Ivers-Tiffée, *J. Power Sources*, **196**, 5342 (2011).
- J. Illig, M. Ender, T. Chrobak, J. P. Schmidt, D. Klotz, and E. Ivers-Tiffée, *J. Electrochem. Soc.*, **159**, A952 (2012).
- D. W. Abarbanel, K. J. Nelson, and J. R. Dahn, *J. Electrochem. Soc.*, **163**, A522 (2016).
- N. Ogihara, Y. Itou, T. Sasaki, and Y. Takeuchi, *J. Phys. Chem. C*, **150**, 102507001 (2015).
- J. N. Illig, *Dr. Diss., Karlsruhe* (2014).
- C. H. Chen, J. Liu, and K. Amine, *J. Power Sources*, **96**, 321 (2001).
- R. Petibon, C. P. Aiken, N. N. Sinha, J. C. Burns, H. Ye, C. M. VanElzen, G. Jain, S. Trussler, and J. R. Dahn, *J. Electrochem. Soc.*, **160**, A117 (2012).
- S. Klink, E. Madej, E. Ventosa, A. Lindner, W. Schuhmann, and F. La Mantia, *Electrochem. commun.*, **22**, 120 (2012).
- M. Ender, A. Weber, and E. Ivers-Tiffée, *J. Electrochem. Soc.*, **159**, A128 (2012).
- C. Bünzli, H. Kaiser, P. Novák, C. Bunzli, H. Kaiser, and P. Novák, *J. Electrochem. Soc.*, **162**, A218 (2014).
- J. Zhou and P. H. L. Notten, *J. Electrochem. Soc.*, **151**, A2173 (2004).
- D. P. Abraham, S. D. Poppen, A. N. Jansen, J. Liu, and D. W. Dees, *Electrochim. Acta*, **49**, 4763 (2004).
- J. L. Gómez-Cámer and P. Novák, *Electrochem. commun.*, **34**, 208 (2013).
- S. Solchenbach, D. Pritzl, E. J. Y. Kong, J. Landesfeind, and H. A. Gasteiger, *J. Electrochem. Soc.*, **163**, A2265 (2016).
- N. Ogihara, S. Kawachi, C. Okuda, Y. Itou, Y. Takeuchi, and Y. Ukyo, *J. Electrochem. Soc.*, **159**, A1034 (2012).
- J. Landesfeind, J. Hattendorff, A. Ehrl, W. A. Wall, and H. A. Gasteiger, *J. Electrochem. Soc.*, **163**, A1373 (2016).
- Andrzej Lasia, *Electrochemical Impedance Spectroscopy and its Applications*, Springer (2014).
- H. Göhr, in *Electrochemical Applications*, p. 2, ZAHNER-elektrik GmbH & Co. KG (1997).
- M. E. Orazem and B. Tribollet, *Electrochemical Impedance Spectroscopy*, WILEY A (2008).
- J. A. Gilbert, J. Bareño, T. Spila, S. E. Trask, D. J. Miller, B. J. Polzin, A. N. Jansen, and D. P. Abraham, *J. Electrochem. Soc.*, **164**, A6054 (2017).
- R. Petibon, J. Xia, L. Ma, M. K. G. Bauer, K. J. Nelson, and J. R. Dahn, *J. Electrochem. Soc.*, **163**, A2571 (2016).
- D. Lu, M. Xu, L. Zhou, A. Garsuch, and B. L. Lucht, *J. Electrochem. Soc.*, **160**, A3138 (2013).
- D. Aurbach, B. Markovsky, Y. Talyossef, G. Salitra, H. J. Kim, and S. Choi, *J. Power Sources*, **162**, 780 (2006).
- B. Michalak, B. B. Berkes, H. Sommer, T. Bergfeldt, T. Brezesinski, and J. Janek, *Anal. Chem.*, **88**, 2877 (2016).
- Y. Dong, J. Demeaux, and B. L. Lucht, *J. Electrochem. Soc.*, **163**, A2413 (2016).
- Matlab Ref., 2016b <https://de.mathworks.com/help/matlab/ref/fminsearch.html>.
- Matlab File Exch., 2016b <http://de.mathworks.com/matlabcentral/fileexchange/13490-adaptive-robust-numerical-differentiation/content/DERIVESTsuite/jacobianest.m>.
- T. Yoon, S. Park, J. Mun, J. Heon, W. Choi, Y. Kang, J. Park, and S. M. Oh, *J. Power Sources*, **215**, 312 (2012).
- D. Pritzl, M. Wetjen, J. Landesfeind, S. Solchenbach, and H. A. Gasteiger, in preparation.
- M. Mohamedi, M. Makino, K. Dokko, T. Itoh, and I. Uchida, *Electrochim. Acta*, **48**, 79 (2002).

34. C. Heubner, M. Schneider, and A. Michaelis, *J. Power Sources*, **288**, 115 (2015).
35. Y.-C. Chang, J.-H. Jong, and G. T.-K. Fey, *J. Electrochem. Soc.*, **147**, 2033 (2000).
36. M. Gaberscek, J. Moskon, B. Erjavec, R. Dominko, and J. Jamnik, *Electrochem. Solid-State Lett.*, **11**, A170 (2008).
37. J. Xia, L. Ma, K. J. Nelson, M. Nie, Z. Lu, and J. R. Dahn, *J. Electrochem. Soc.*, **163**, 2399 (2016).
38. A. Ehrl, J. Landesfeind, W. A. Wall, H. A. Gasteiger, and W. A. Wall, *J. Electrochem. Soc.*, **164**, A826 (2017).
39. M. Park, X. Zhang, M. Chung, G. B. Less, and A. M. Sastry, *J. Power Sources*, **195**, 7904 (2010).
40. V. F. Lvovich, *Impedance Spectroscopy Applications to Electrochemical and Dielectric Phenomena*, p. 78, John Wiley & Sons, Ltd, New Jersey (2012).